Scripta Materialia 231 (2023) 115430

Contents lists available at ScienceDirect

Scripta Materialia

journal homepage: www.journals.elsevier.com/scripta-materialia

Solidification microstructure variations in additively manufactured Ti-6Al-4V using laser powder bed fusion

Lu Yang [a], Saranarayanan Ramachandran [a], Axieh Bagasol [b], Qiyu Guan [a], Weiguang Wang [c], David J. Browne [b], Denis Dowling [b], Wajira Mirihanage [a,*]

[a] Department of Materials, The University of Manchester, Manchester M13 9PL, UK
[b] School of Mechanical & Materials Engineering, University College Dublin, Belfield, Dublin 4, Ireland
[c] Department of Mechanical, Aerospace and Civil Engineering, The University of Manchester, Manchester M13 9PL, UK

ARTICLE INFO

Keywords:
Additive manufacturing
Grain orientation
Parent phase

ABSTRACT

Laser powder bed fusion (LPBF) offers unique opportunities to produce metallic components without conventional design and manufacturing constraints. During additive manufacturing process, titanium alloys like Ti-6Al-4V undergo solid-state transformation that conceals initial solidification microstructure from room-temperature observations. Revealing the as-solidified microstructure can be critical to understanding the early stages of solidification. Using orientation relationships between parent (α) and child (β) phases, the as-solidified microstructures across the LPBF build volume has been reconstructed. Based on the as-solidified parent phase information, variations of the thermal and solidification conditions that occur during the LPBF of Ti-6Al-4V are revealed. The results show that how high cooling rates in the initially solidified lower layers contributed to orientation distribution during parent phase solidification, compared to upper layers in the build volume. Furthermore, the approach demonstrates the potential to further explore solidification microstructure and defect formation in titanium alloys during additive manufacturing.

Titanium alloys are widely utilized in the fields of aerospace, transportation and biomedical engineering [1]. Ti-6Al-4V (wt.%) is a popular titanium alloy owing to its high strength-to-weight ratio, biocompatibility and good fatigue resistance [1,2]. Additive manufacturing (AM) is becoming increasingly popular with its enhanced design flexibility and tooling advantages [3–5]. Laser powder bed fusion (LPBF) is a widely applied AM technique characterized by layer-by-layer scanning of a high-energy laser beam [4]. During LPBF, metallic powders are rapidly melted by a laser, then solidified and cooled to room temperature. Solid-solid phase transformations also occur during this process [6]. The solidification process, greatly influenced by the processing parameters and thermal conditions, is of vital importance for the final microstructure and part quality. However, research to date on AM of Ti-6Al-4V and similar titanium alloys has been mainly focused on the analysis of the final room-temperature microstructure, rather than the as-solidified microstructure and relevance to the solidification conditions [6–8].

In general, the Ti-6Al-4V microstructure above β-transus temperature (around 1000 °C) is dominated by relatively large prior or parent β grains [9,10]. According to the Continuous Cooling Transformation (CCT) diagram for Ti-6Al-4V [11], the transformed microstructure present at room temperature would be observed as lamellar α and β phase at moderate cooling rate, or interwoven martensitic α' laths with a tiny number of equiaxed β grains when the cooling rate is high (i.e. 10^3 and 10^8 K s^{-1}, respectively, for the LPBF process) [7,12,13]. The phase transformation between the parent body-centred cubic (bcc) β phase matrix and child hexagonal close-packed (hcp) α phase obeys the Burgers Orientation Relationship (BOR) which is based on two parallel planes $\{110\}_\beta//(0001)_\alpha$ and two parallel directions $<111>_\beta//<2\text{-}1\text{-}10>_\alpha$ in α and β phase. Due to the crystal symmetry of both phases, there are 12 distinct variants for the child α phase transformed from a single parent β grain [12,14,15]. Notably, both α and α' phase have hcp crystal structure and obey BOR during phase transformation [16]. Thus, the reconstruction process, which we consider here for α phase, is also valid for any α' phase present.

The Ti-6Al-4V microstructure formed during the solidification process cannot be directly observed via the final microstructure at room temperature [17]. However, examination of the as-solidified microstructure will enhance the capability to control the LPBF process, which

* Corresponding author.
E-mail address: wajira.mirihanage@manchester.ac.uk (W. Mirihanage).

https://doi.org/10.1016/j.scriptamat.2023.115430
Received 9 November 2022; Received in revised form 6 February 2023; Accepted 13 March 2023
Available online 27 March 2023

enables the elimination of solidification defects that persist as the build cools further to ambient conditions. Here we study the as-solidified Ti-6Al-4V microstructure formed during the LPBF process using the crystallographic relationships between parent and child phases [12,14,17], and enabled by the Electron Backscatter Diffraction (EBSD) data.

In this contribution, extra-low interstitial (ELI), grade 23 Ti-6Al-4V alloy powders of ASTM B348-19 with powder sizes in the range of 21–48 μm were deposited with the Renishaw 500S® AM system. The build plate was preheated and kept at 170°C during the process. The laser power, hatch spacing, layer thickness, exposure time and point distance were respectively 400 W, 100 μm, 60 μm, 60 μs and 80 μm, and the build volume was 250 × 250 × 170 mm^3. Cylindrical samples of 12 mm diameter were initially extracted from positions 10, 140 and 235 mm away from the right edge of the build plate. The horizontal locations are regarded as 'Right', 'Middle' and 'Left' respectively in this configuration (for more details, see supplementary Fig. S1 and Ref. [18]). In each location, samples were extracted from approximately 15 mm and 155 mm distance from the build plate, and these vertical locations are regarded as 'Top' and 'Bottom'. The laser moved from right to left during the layer-by-layer additive process.

From these six locations, extracted disc-shaped sample slices were mounted in hot-mounting resin, and ground on silicon carbide abrasive papers with grit sizes from 240 to 2400 (μm). Afterwards, samples were polished with 6, 1, 1/4 μm diamond paste and with OPUS® colloidal silica. EBSD images were obtained using the TESCAN® Mira3® electron microscope. The accelerating voltage, beam current and scanning step size were respectively set as 20 kV, 11 μA and 0.25 μm. The Aztec® 5.1 software was used for data collection and initial data processing.

The MATLAB® MTEX toolbox was employed to implement the BOR relationship and reconstruct the parent β phase microstructure and pole figures from the EBSD details of the room-temperature child α and α' phases, using the approach detailed in Ref. [19]. A given threshold of grain boundary angle was employed to identify grain boundaries and to achieve a desirable reconstruction rate for the results presented here. Then the reconstructed grains were merged to become larger grains based on the consideration of misorientation angles. The grain size and the primary dendrite (grain) spacing, λ of the reconstructed grains were measured using the software NIH-Image/ImageJ. The relationship between the λ (μm) and cooling rate, $\dot{T}$ (K/s) for Ti-6Al-4V has been established [20] as;

$$\lambda = 3.1 \times 10^{6} \dot{T}^{-1.05} \quad (1)$$

The room-temperature microstructures in the six locations were observed on sample cross-sections (looking down from the top of the build sample) using EBSD images, and representative microstructures for each location are shown in Fig. 1 (the supplementary phase maps and misorientation profiles of the selected locations are presented in Fig. S3). The microstructures (shown in Fig. 1) are dominated by the basket-weave and needle-shaped laths microstructure consist of α/α' phase, which take up approximately 99% of the field of view. This can be attributed to the high $\dot{T}$ encountered during the process [12,21,22]. In Fig. 1, clusters of basket-weave and needle-shaped grains can be seen. The grains in a single α/α' cluster with a similar orientation are generally assumed as the grains that transformed from one parent β grain [23].

The reconstructed microstructures of the parent β phase using the BOR relationship (from Fig. 1 child phase) are presented in Fig. 2. The orientations of large β grains vary considerably from location to location. During the reconstruction of the parent β phase which was implemented in the MTEX toolbox, two main parameters, the threshold grain boundary angle and misorientation angle, allow the provision of more rational rendering. 3° threshold grain boundary angle and 5° misorientation angle were chosen as the optimum parameters that achieved the 100% reconstruction rate with minimum angles just above the orientation noise floor for separating grains [19].

To further detail the as-solidified β grain orientations, (001) pole figures were created as shown in Fig. 3. (001) is the preferred crystallographic growth direction for the bcc crystals (e.g. Ti-β phase), and the microstructures were obtained from the planar-cross sections. Thus, these pole figures generally represent the projected view of the growth directions. For example, the centre of the pole figure (any circle) indicates the grain(s) that grow directly upward. As displayed by the reconstructed as-solidified microstructures, orientation distributions are relatively random in the 'Left-Bottom' and 'Middle-Bottom' locations. Compared to these two locations, less orientation scatter can be observed in other locations, as evident from Fig. 3. This variation is related to grain number density as well as measured grain sizes presented in Fig. 4a. For example, in Fig. 3b ('Middle-Top' location), there are a small number of orientations with large grain sizes concentrating around three directions, which indicate slightly offset growth direction

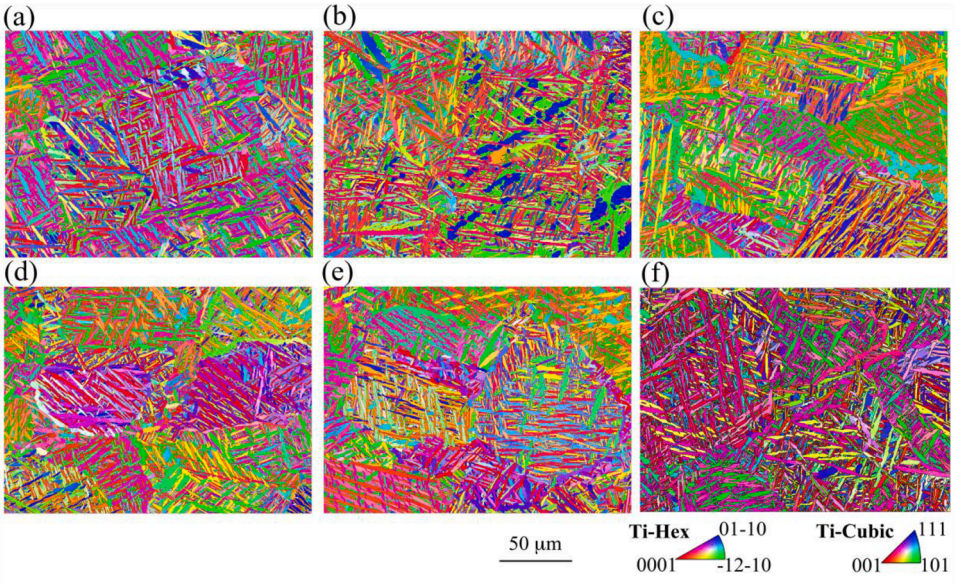

Fig. 1. EBSD images for the final room-temperature microstructure view from the top side of Ti-6Al-4V produced by LPBF. (a) 'Left-Top' location. (b) 'Middle-Top' location. (c) 'Right-Top' location. (d) 'Left-Bottom' location. (e) 'Middle-Bottom' location. (f) 'Right-Bottom' location.

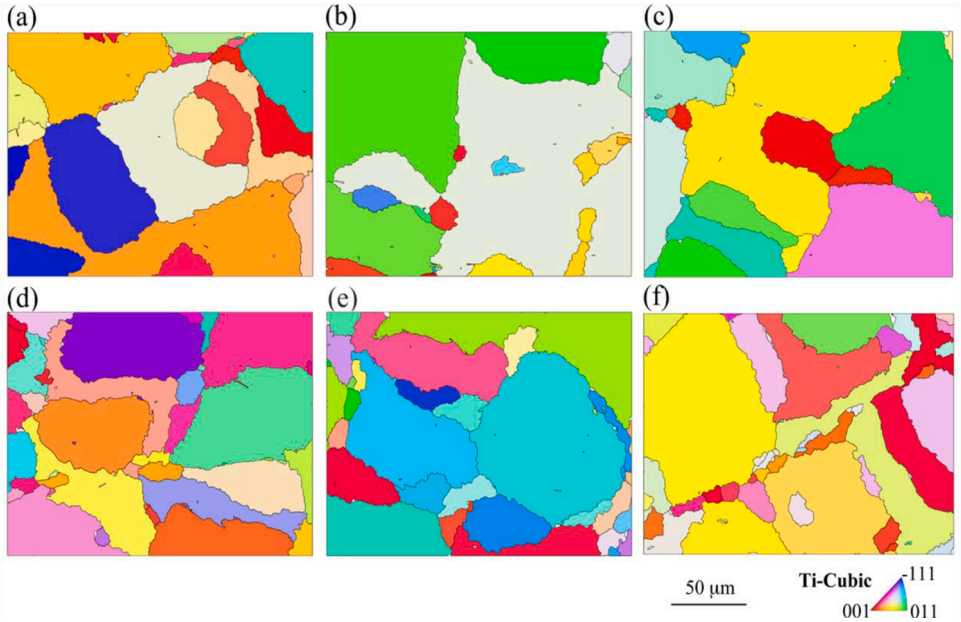

Fig. 2. EBSD images for reconstructed parent microstructure of Ti-6Al-4V produced by LPBF. (a) 'Left-Top' location. (b) 'Middle-Top' location. (c) 'Right-Top' location. (d) 'Left-Bottom' location. (e) 'Middle-Bottom' location. (f) 'Right-Bottom' location.

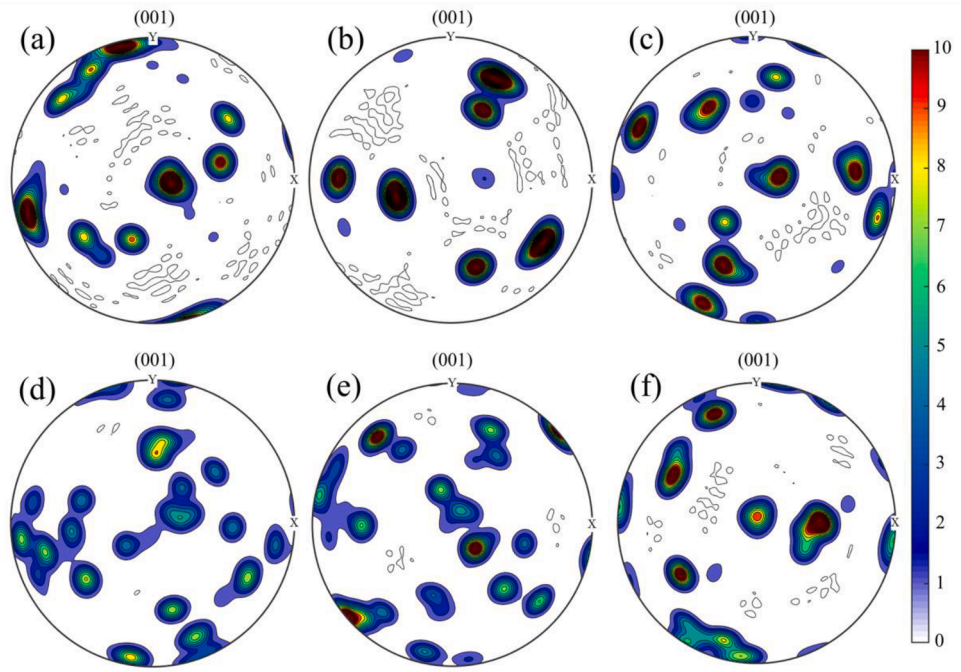

Fig. 3. Pole figures (001) for reconstructed parent microstructure of Ti-6Al-4V produced by LPBF. (a) 'Left-Top' location. (b) 'Middle-Top' location. (c) 'Right-Top' location. (d) 'Left-Bottom' location. (e) 'Middle-Bottom' location. (f) 'Right-Bottom' location.

to the upward. In contrast, in the 'Left-Bottom' (Fig. 3d) and 'Middle-Bottom' locations (Fig. 3e), the grain sizes are relatively small and the orientation distributions are more random compared to the location 'Right-Bottom'.

The average grain size (equivalent diameter) of the room-temperature microstructure (Fig. 1) is less than 10 μm, but some α/α'-laths with large aspect ratios can have equivalent grain size up to 50 μm. But no extensive differences in the attributes of different locations can be directly observed. Thus, apparently, room-temperature microstructures show good homogeneity across the build volume. Generally, reconstructed parent β grains are several times larger than the child (both α and α') grains, and show an extensive size range in all sample locations but only moderate differences in the average size, or more accurately cross-sections, appear as shown in Fig. 4a. However, higher contrast in grain sizes (room-temperature microstructure) is clear when the grain orientations are taken into consideration using the pole figures as shown in Fig. 3. When the parent grain structure is generated during the solidification, cooling conditions dominate the microstructure formation. The local thermal gradient (G) influences the growth direction, while the cooling rate controls the spacing between grains that grow along a similar direction. Thus, as presented in Fig. 4b, $\dot{T}$ during the solidification can be estimated by applying Eq. (1) to the

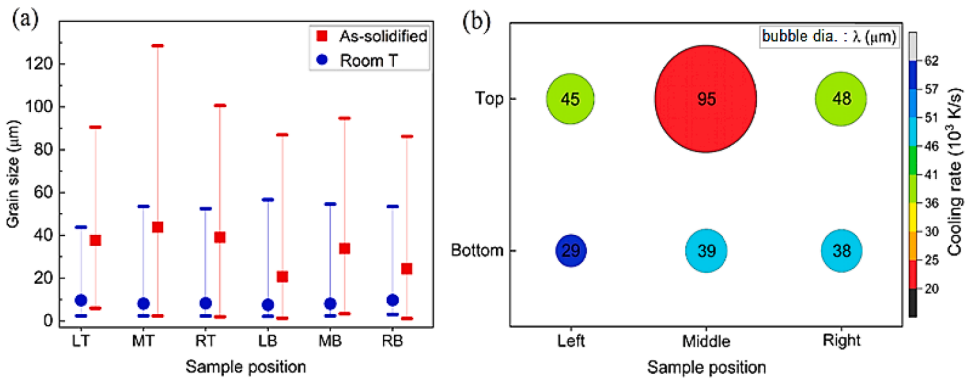

Fig. 4. (a) Average grain cross-section size (maximum and minimum values are denoted with error bars): child α/α' (room-temperature) and reconstructed parent β (as-solidified). (b) Grain spacing (bubble diameter) and cooling rates (bubble colour) for reconstructed parent β microstructure, by location.

measured λ. With the orientation details, λ was obtained by taking adjoining grains, with near parallel growth orientations (i.e., similar colours in Fig. 2), into account. As indicated in Figs. 2 and 3 (and directly shown in supplementary Fig. S2), most of the β appear to have solidified as columnar grains. Such grains grow under high thermal gradients either epitaxially from existing solid or nucleate in the melt. With highly dynamic thermal conditions, the variation of thermal gradients within the melt pool on a mesoscopic scale may allow grains to grow along localised higher thermal gradients [24]. Flow-driven conditions can dynamically change the growth orientations considerably [25,26], to develop these as-solidified microstructures.

When this LPBF process is considered, the laser started scanning from 'Right-Bottom' towards 'Left-Bottom' of the build volume, then repeated the same pattern while building the upper layers. The heat added during the processing of the lower layers would reduce the effective cooling rate of the upper layers. It is noteworthy that the cooling rates in 'Middle' locations are lower compared to 'Right' and 'Left' locations in both the 'Top' and 'Bottom' layers. The quantified cooling rate observations here are consistent with the trend reported in the comparable simulation results in Refs. [27,28]. The estimated cooling rate variations, particularly lower values, are possibly associated with the limited heat dissipation potential in central locations, which are surrounded by hot and just-solidified metal, while the thermal distributions in 'Right' and 'Left' locations reflect the proximity to relatively cold and un-fused loose powder or the build plate, which can cool fast.

Both $\dot{T}$ and the temperature gradient G significantly affect the microstructure formation. The higher $\dot{T}$ can mainly stimulate more constitutional undercooling and nucleation, while the higher G can promote the columnar morphology that prefers to grow along the direction of the highest G [24,29,30]. The estimated $\dot{T}$ range is between 20 to 60 $\times$ 10^3 K/s, consistent with the values reported in Ref. [31]. As observed here (Fig. 4b), $\dot{T}$ in 'Bottom' locations are higher than those of 'Top' locations. Thus, compared to the 'Top' locations in Fig. 3, there are more grains with scattered orientations in the 'Left-Bottom' and 'Middle-Bottom'. In this study, the laser scans started near the 'Right-Bottom'. Thus, relative to other locations, G could be higher in the 'Right-Bottom' due to lower residual heat. Consequently, grains in the 'Right-Bottom' location have a higher propensity to form columnar grains with limited orientation distribution (Fig. 3f). Both $\dot{T}$ and G in 'Top' locations are relatively lower due to the heat build-up during the printing of lower layers. Therefore, the grain sizes (projected columnar cross-sections) and estimated λ in 'Top' locations are higher as shown in Fig. 4, with lesser scatter in growth orientation (Fig. 3a-c). Heat dissipation in the 'Right-Top' location occurs through layers below and the nearby right edge, where the heat transfer through loose powder would not be as efficient as through solid metal. Therefore, variation of a maximum thermal gradient, both the magnitude and the direction, in the undercooled regions of the melt pool can vary. In this contribution, we demonstrate the relatively straightforward solidification conditions that can be expected at edge locations of the build volume. For the more central regions of the build volume, which would be affected by multi-directional heat flow, and further study of more complicated solidification conditions could be completed in extended research. However, in this paper we demonstrate the approach to be taken.

Based on the consideration of the overall microstructure, despite the large build volume, room-temperature final microstructures are considerably homogeneous when the final α/α'-laths sizes are concerned. However, parent solidification microstructures indicate interesting solidification variations across the build volume. Notably, these process condition variations are visible only when the as-solidified parent microstructures are taken into account. As-solidified microstructure can be affected during the subsequent deposition of upper layers, if the re-melting occurs considerably. Nevertheless, very limited re-melting typically involves with LPBF. In addition, Ti-6Al-4V has lower thermal conductivity. Thus, it is reasonable to suppose no significant microstructure alterations happen in our considered location due to the deposition of subsequent layers. With such consideration, the example here reveals the diverse solidification conditions that can appear across Ti-6Al-4V additively manufactured build volumes, but may not be directly apparent or understandable from conventional room-temperature microstructural investigations. The reconstruction and analysis of the solidification, as demonstrated in this letter, can be employed to study microstructure evolution and defect formation during additive manufacturing of metallic alloys (i.e. titanium and steels) that undergo solid-state phase transformation at high temperatures. Similar research has also been reported with [32,33] for other metal processing methods.

To conclude, we reveal the solidification conditions during an AM process of Ti-6Al-4V alloy employing crystallographic relationships between the child and parent phases. The results reveal distinctive thermal conditions ensue during the sequence of liquid-solid transformation across the LPBF build volume. These thermal conditions are not directly reflected from the room-temperature microstructure (after liquid → β and β → α/α' transformations). This highlights the importance of considering the multiple-phase transformation sequences and their attributes in establishing process-structure relations for alloys like Ti-6Al-4V during AM processes. The revealed primary solidification grain structure can also be used to validate the solidification models or study the solidification related defeat formation during AM of Ti alloys.

Declaration of Competing Interest

The authors declare that they have no known competing financial interests or personal relationships that could have appeared to influence the work reported in this paper.

Acknowledgements

The authors acknowledge support from the EPSRC, UK (Grant No. EP/R031711/1) and Science Foundation Ireland (Grant number 16/RC/3872). For the purpose of Open Access, the author has applied a CC BY public copyright licence to any Author Accepted Manuscript version arising from this submission.

Supplementary materials

Supplementary material associated with this article can be found, in the online version, at doi:10.1016/j.scriptamat.2023.115430.

References

[1] X. Zhao, S. Li, M. Zhang, Y. Liu, T.B. Sercombe, S. Wang, Y. Hao, R. Yang, L. E. Murr, Comparison of the microstructures and mechanical properties of Ti–6Al–4V fabricated by selective laser melting and electron beam melting, Mater. Des. 95 (2016) 21–31.
[2] C.W. Kang, F.Z. Fang, State of the art of bioimplants manufacturing: part I, Adv. Manuf. 6 (2018) 20–40.
[3] V.S. Telang, R. Pemmada, S. Ramakrishna, P. Tandon, H.S. Nanda, Overview of Current Additive Manufacturing Technologies for Titanium Bioimplants, in: L.M. Pandey, A. Hasan (Eds.), Nanoscale Engineering of Biomaterials: Properties and Applications, Springer Nature, Singapore, 2022, 117-130.
[4] L.C. Zhang, H. Attar, Selective laser melting of titanium alloys and titanium matrix composites for biomedical applications: a review, Adv. Eng. Mater. 18 (2016) 463–475.
[5] W. Zhang, D. Guo, L. Wang, C.M. Davies, W. Mirihanage, M. Tong, N.M. Harrison, X-ray diffraction measurements and computational prediction of residual stress mitigation scanning strategies in powder bed fusion additive manufacturing, Addit. Manuf. 61 (2023), 103275.
[6] J. Li, X. Zhou, M. Brochu, N. Provatas, Y.F. Zhao, Solidification microstructure simulation of Ti-6Al-4V in metal additive manufacturing: A review, Addit. Manuf. 31 (2020), 100989.
[7] A.M. Khorasani, I. Gibson, M. Goldberg, G. Littlefair, A survey on mechanisms and critical parameters on solidification of selective laser melting during fabrication of Ti-6Al-4V prosthetic acetabular cup, Mater. Des. 103 (2016) 348–355.
[8] S. Yamamoto, H. Azuma, S. Suzuki, S. Kajino, N. Sato, T. Okane, S. Nakano, T. Shimizu, Melting and solidification behavior of Ti-6Al-4V powder during selective laser melting, Int. J. Adv. Manuf. Tech. 103 (2019) 4433–4442.
[9] A. Gomez-Gallegos, P. Mandal, D. Gonzalez, N. Zuelli, P. Blackwell, Studies on titanium alloys for aerospace application, Defect Diffus. Forum. 385 (2018) 419–423.
[10] S. Tamirisakandala, R.B. Bhat, D.B. Miracle, S. Boddapati, R. Bordia, R. Vanover, V. K. Vasudevan, Effect of boron on the beta transus of Ti–6Al–4V alloy, Scr. Mater 53 (2005) 217–222.
[11] C. Zhong, J. Liu, T. Zhao, T. Schopphoven, J. Fu, A. Gasser, J.H. Schleifenbaum, Laser metal deposition of Ti6Al4V—a brief review, Appl. Sci. 10 (2020) 764.
[12] P. Kumar, U. Ramamurty, Microstructural optimization through heat treatment for enhancing the fracture toughness and fatigue crack growth resistance of selective laser melted Ti6Al4V alloy, Acta Mater 169 (2019) 45–59.
[13] H. Ali, L. Ma, H. Ghadbeigi, K. Mumtaz, In-situ residual stress reduction, martensitic decomposition and mechanical properties enhancement through high temperature powder bed pre-heating of Selective Laser Melted Ti6Al4V, Mater. Sci. Eng. A. 695 (2017) 211–220.
[14] M.G. Glavicic, P.A. Kobryn, T.R. Bieler, S.L. Semiatin, A method to determine the orientation of the high-temperature beta phase from measured EBSD data for the low-temperature alpha phase in Ti-6Al-4V, Mater. Sci. Eng. A. 346 (2003) 50–59.
[15] M. Humbert, H. Moustahfid, F. Wagner, M.J. Philippe, Evaluation of the high temperature texture of the [Beta] phase of a TA6V sample from the individual orientations of grains of the low temperature [alpha] phase, Scr. Mater. 30 (1994) 377–382.
[16] H.Z. Zhong, Z. Liu, J.F. Gu, The vertical and triangular morphology in the as-deposited Ti-6Al-4V, Mater. Charact. 131 (2017) 91–97.
[17] P.S. Davies, B.P. Wynne, W.M. Rainforth, M.J. Thomas, P.L. Threadgill, Development of microstructure and crystallographic texture during stationary shoulder friction stir welding of Ti-6Al-4V, Metall. Mater. Trans. A. 42 (2011) 2278–2289.
[18] A.J. Bagasol, F.R. Kaschel, S. Ramchandran, W. Mirihanage, D. Browne, D.P. Dowling, The influence of a large build area on the microstructure and mechanical properties of PBF-LB Ti-6Al-4V alloy, Int. J. Adv. Manuf. Technol. 125 (2023) 1355–1369.
[19] F. Niessen, T. Nyyssönen, A.A. Gazder, R. Hielscher, Parent grain reconstruction from partially or fully transformed microstructures in MTEX, J. Appl. Crystallogr. 55 (2022) 180–194.
[20] L. Wu, J. Zhang, Phase field simulation of dendritic solidification of Ti-6Al-4V during additive manufacturing process, JOM 70 (2018) 2392–2399.
[21] T. Vilaro, C. Colin, J.D. Bartout, As-fabricated and heat-treated microstructures of the Ti-6Al-4V alloy processed by selective laser melting, Metall. Mater. Trans. A. 42 (2011) 3190–3199.
[22] Z. Xie, Y. Dai, X. Ou, S. Ni, M. Song, Effects of selective laser melting build orientations on the microstructure and tensile performance of Ti–6Al–4V alloy, Mater. Sci. Eng. A. 776 (2020), 139001.
[23] B. Vrancken, L. Thijs, J.P. Kruth, J. Van Humbeeck, Heat treatment of Ti6Al4V produced by Selective Laser Melting: Microstructure and mechanical properties, J. Alloys Compd. 541 (2012) 177–185.
[24] A.T. Polonsky, W.C. Lenthe, M.P. Echlin, V. Livescu, G.T. Gray III, T.M. Pollock, Solidification-driven orientation gradients in additively manufactured stainless steel, Acta Mater 183 (2020) 249–260.
[25] W.U. Mirihanage, M. Di Michiel, A. Reiten, L. Arnberg, H.B. Dong, R.H. Mathiesen, Time-resolved X-ray diffraction studies of solidification microstructure evolution in welding, Acta Mater 68 (2014) 159–168.
[26] N. Shevchenko, O. Roshchupkina, O. Sokolova, S. Eckert, The effect of natural and forced melt convection on dendritic solidification in Ga–In alloys, J. Crystal Growth. 417 (2015) 1–8.
[27] Y. Li, K. Zhou, P. Tan, S.B. Tor, C.K. Chua, K.F. Leong, Modeling temperature and residual stress fields in selective laser melting, Int. J. Mech. Sci. 136 (2018) 24–35.
[28] Y. Du, X. You, F. Qiao, L. Guo, Z. Liu, A model for predicting the temperature field during selective laser melting, Results Phys 12 (2019) 52–60.
[29] M.A. Easton, D.H. StJohn, Improved prediction of the grain size of aluminum alloys that includes the effect of cooling rate, Mater. Sci. Eng. A. 486 (2008) 8–13.
[30] W.U. Mirihanage, H.J. Dai, H.B. Dong, D.J. Browne, Computational Modeling of Columnar to Equiaxed Transition in Alloy Solidification, Adv. Eng. Mater. 15 (2013) 216–229.
[31] S. Pauly, P. Wang, U. Kühn, K. Kosiba, Experimental determination of cooling rates in selectively laser-melted eutectic Al-33Cu, Addit. Manuf. 22 (2018) 753–757.
[32] Z.B. Zhao, Q.J. Wang, Q.M. Hu, J.R. Liu, B.B. Yu, R. Yang, Effect of β (110) texture intensity on α-variant selection and microstructure morphology during β→ α phase transformation in near α titanium alloy, Acta Mater 126 (2017) 372–382.
[33] C. Cayron, B. Artaud, L. Briottet, Reconstruction of parent grains from EBSD data, Mater. Charact. 57 (2006) 386–401.